Volume 15
Number 40
28 October 2023
Pages 16231-16502

Nanoscale

rsc.li/nanoscale

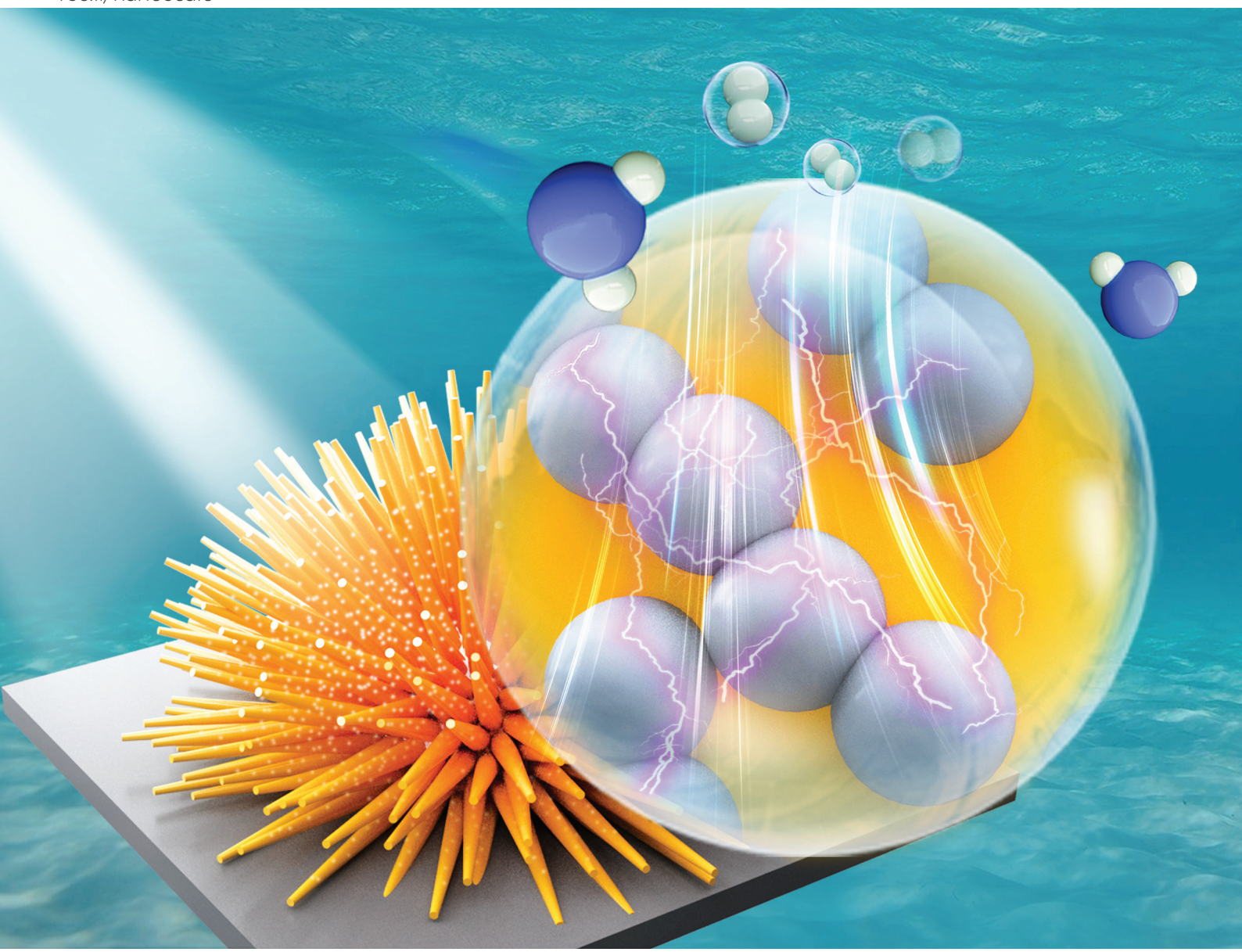

ISSN 2040-3372

ROYAL SOCIETY OF CHEMISTRY

PAPER

Yang Jin, Yunfei Xie, Young Mee Jung *et al.*
Ag decoration on $Na_2Ti_3O_7$ nanowires for improved SERS and PHE performance

NCNST

Nanoscale

PAPER

View Article Online
View Journal | View Issue

Cite this: *Nanoscale*, 2023, **15**, 16287

Ag decoration on $Na_2Ti_3O_7$ nanowires for improved SERS and PHE performance†

Lei Chen,[a] Yang Jin,*[b] Shuang Guo,[c] Eungyeong Park,[c] Yunfei Xie *[b] and Young Mee Jung *[c]

Received 10th August 2023,
Accepted 11th September 2023

DOI: 10.1039/d3nr03994c

rsc.li/nanoscale

$Na_2Ti_3O_7$ (NTO) is recognized as an authenticated promising photocatalyst and surface-enhanced Raman scattering (SERS) active material, although its performance is limited by its high carrier recombination rate, wide band gap and inadequate utilization of visible light. In this study, to solve these issues, sea urchin-shaped NTO nanowires directly grown on a substrate were fabricated, and then Ag nanoparticles were decorated on NTO nanowires using sputtering equipment. The as-prepared Ag-NTO substrates exhibited different morphologies and high SERS activity, which was confirmed by finite-difference time-domain (FDTD) simulations, showing that appropriate Ag decoration can bring more nanogaps and thus enhance the electromagnetic field (EM) contribution. We visualized the charge transfer (CT) mechanism in SERS and further investigated the catalytic hydrogen production process similarly induced by photogenerated CT. The optimal SERS substrate (Ag-NTO-3) was adopted to verify the photocatalytic hydrogen evolution (PHE) activity, and the hydrogen evolution rate of Ag-NTO-3 was 106.7 μmol h^{-1} (twice that of pristine NTO). Photoelectrochemical measurements and photoluminescence (PL) analysis were used to elucidate the potential enhancement mechanisms for the photocatalytic performance and CT process. This study can provide a valuable reference for performance and mechanism studies of SERS substrates and photocatalysts.

1 Introduction

The design of a surface-enhanced Raman scattering (SERS) substrate material is recognized as a significant contributing factor to the surface enhancement effect. Common SERS active materials, *i.e.*, noble and transition metals, have had limited application due to their inherent characteristics, including high cost, poor stability, lack of reproducibility, and low biocompatibility.[1] Semiconductor-based SERS substrates, due to their tunable energy band structure, relatively low cost, good absorption capacity, and selective enhancement properties, can be used to precisely identify target molecules in complex environments.[2] Compared to the individual use of pure metals or semiconductors, the combination of these materials has tremendously expanded SERS applications, as there are great advantages in terms of the Raman intensity, charge transfer (CT) efficiency, catalytic activity, and recyclability.[3–5] Surface plasmon resonance (SPR) and CT, which are enhancements occurring independently in both materials, cooperatively contribute to the SERS response in composite materials.

$Na_2Ti_3O_7$ (NTO), a TiO_2-based alkali metal titanate semiconductor, has attracted increasing attention due to its high chemical inertness, nontoxicity, ion exchangeability, and low cost.[6,7] However, the existence of a wide band gap limits the light absorption range and facilitates the recombination of photogenerated electron–hole pairs on the surface.[8] These drawbacks have been addressed by various modification strategies, such as metal- or nonmetal-doping sensitization, noble metal deposition, and other suitable semiconductor coupling methods. Plasmonic metals are believed to be prospective photocatalysts due to the localized surface plasmon resonance (LSPR), which improves the absorption of visible light by trapping photoexcited charges through Schottky junctions.[9,10] The formed high-energy hot electrons can access the surface of plasmonic particles and directly participate in the photocatalytic reaction at the femtosecond level.[11] Noble metal nanoparticles (NPs) that are widely used as surface modifiers for TiO_2-based photocatalysts act as "electron slots" to reduce charge recombination, improving the photoreduction efficiency.[12,13] For the composite structure, the enhanced local electromagnetic field caused by LSPR improves the carrier mobility and the polarization effect on adsorbed molecules,

[a]*School of Materials Science and Engineering, Jilin Jianzhu University, Changchun 130118, China*
[b]*School of Food Science and Technology, Jiangnan University, Wuxi, Jiangsu 214122, China. E-mail: jy1165254033@163.com, xieyunfei@jiangnan.edu.cn*
[c]*Department of Chemistry, Institute for Molecular Science and Fusion Technology, Kangwon National University, Chunchon 24341, Korea. E-mail: ymjung@kangwon.ac.kr*

† Electronic supplementary information (ESI) available. See DOI: https://doi.org/10.1039/d3nr03994c

providing rich active sites.[14] In composite nanomaterials, the Schottky barriers between plasmonic metals and semiconductors ensure the efficient transport of photoelectrons, bringing high-energy electrons to the catalytic sites, and extending the carrier lifetime.[15] Reasonable morphology design of titanates, such as nanowires, nanoribbons, nanosheets, and nanotubes, can induce greater enhancement because the larger the surface area is, the more metal NPs can be attached. Besides, the introduction of the noble metal can improve the SERS and photocatalyst activity which is due to the LSPR effect. Khanam's group fabricated the Ag/Bi_2WO_6 nanostructure and produced 6.608 μmol min^{-1} H_2.[16] Yang *et al.* constructed Ag/TiO_2 core–shell nanoparticles and reached a 10^{-10} detection concentration for MBA.[17] In the cases of $Ag@MoS_2$ composite with a 1736 μmol h^{-1} g^{-1} maximum hydrogen production rate and a 5.2×10^9 high enhancement factor of three-dimensional (3D) Ag-TiO_2 nanowires, decorating Ag provides the additional improvement of the SERS and PHE performance.[18,19]

Powder photocatalysts have high photocatalytic activity but have the disadvantages that the separation process from the reaction solution is complicated and the photocatalytic activity is reduced due to the agglomeration of large powder after recycling.[20] In this study, we fabricated NTO nanowires grown directly on Ti sheets through a hydrothermal reaction, which improves on the disadvantages of powder photocatalysts. Ag NPs were then deposited on NTO nanowires through the magnetron sputtering technique, and the surface morphology of Ag-NTO substrates was adjusted according to the sputtering power. This special composite nanostructure has a strong electromagnetic field and abundant SERS hot spots. Furthermore, the optimal SERS substrate also exhibits excellent performance for photocatalytic hydrogen evolution (PHE).

We analyzed the enhancement mechanisms for both SERS and the photocatalytic activity through the CT process and clearly confirmed that the enhanced SERS activity and photocatalytic hydrogen production performance was attributed to the Ag cover.

2 Experimental

2.1 Preparation of substrate materials

2.1.1 Growth of NTO nanowires. NTO nanowire structures were grown on Ti sheets using a hydrothermal reaction. The 3 cm × 3 cm Ti sheets were ultrasonically cleaned with ethanol, hydrochloric acid, and deionized water for 10 min each in turn to remove organic pollutants and the oxidized layer and then immersed in deionized water. Next, 25 mL of NaOH solution with a concentration of 1 M was added to a high-pressure tank lined with polytetrafluoroethylene to react with the cleaned Ti sheets at 180 °C for 48 h to obtain NTO nanowire arrays. The reacted sheets were ultrasonically cleaned with deionized water and dried in a vacuum drying oven for further magnetron sputtering. Experimental diagram is illustrated in Scheme 1.

2.1.2 Ag decoration on NTO nanowires. The magnetron sputtering equipment was used to decorate Ag NPs on NTO nanowires. The Ag target was mounted on the magnetic target position in the sputtering chamber with a 0° target deflection angle, and the background air pressure was lower than 0.2 Pa before starting. When sputtering, we controlled the Ar gas flow and lowered the molecular pump to keep the working air pressure at 0.6 Pa. The Ag sputtering power was 10, 20, 30, and 40 W, and the sputtering time was set to 30 s. These prepared substrates were labeled Ag-NTO-1, Ag-NTO-2, Ag-NTO-3, and Ag-NTO-4, respectively. These different substrates were immersed in a 10^{-3} M solution of 4-mercaptobenzoic acid (4-MBA), chosen as the Raman probe molecule, for 30 min at room temperature, then rinsed with deionized water and dried under vacuum conditions.

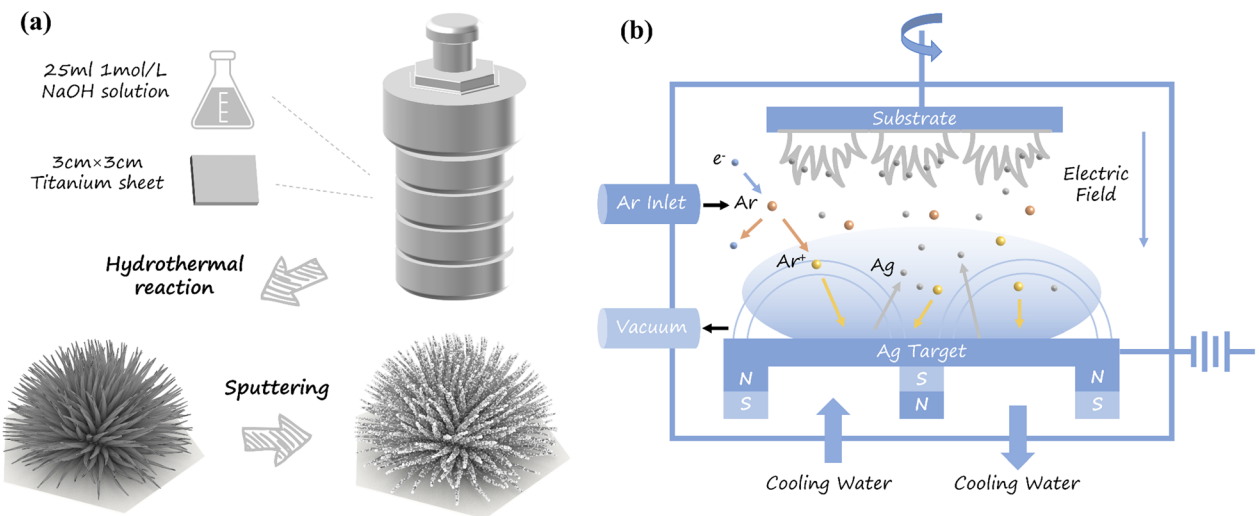

Scheme 1 Schematic depiction of the (a) experimental procedures and (b) sputtering diagram.

2.2 Photocatalytic hydrogen evolution (PHE)

The PHE reaction was carried out under visible light (100 mW cm^{-2}, 350 W Xe lamp, λ > 420 nm) and atmospheric conditions. Triethanolamine (TEOA, 10 wt%) was used as a sacrificial agent, and 3 wt% Pt produced by $H_2PtCl_6{\cdot}6H_2O$ was used as a cocatalyst. The air in the reaction system was completely evacuated with Ar before irradiation, and the temperature of the solution was maintained at approximately 18 °C by a flow of cooling water during the entire process. The H_2 production rate was detected *via* gas chromatography (GC-2014, Shimadzu).

2.3 Photoelectrochemical (PEC) measurement

An electrochemical workstation (CHI600E, CH Instruments, Inc.) was employed to perform the photocurrent response (PCR), electrochemical impedance spectroscopy (EIS), and Mott–Schottky measurements. Based on the three-electrode system, a saturated calomel electrode, a Pt electrode and an as-prepared substrate were used as the reference electrode, auxiliary electrode, and working electrode, respectively. The EIS plots were recorded in the frequency range of 0.1–10^6 Hz in 10 mM $Fe[(CN)_6]^{3-/4-}$ aqueous solution. PCR and Mott–Schottky results were obtained in a 0.5 M Na_2SO_4 electrolyte solution at 0 V bias or in a voltage range of −1.5–1 V with an amplitude of 10 mV.

3 Results and discussion

Fig. 1 shows the X-ray diffraction (XRD) patterns of the prepared substrates. All the diffraction peaks of the Ti sheet can be indexed to hexagonal Ti crystals (JCPDS card No. 44-1294). The Ti peaks at 53.0° and 70.6° are prominent in every sample. For NTO nanowires, all diffraction peaks correspond to hexagonal Ti crystals and monoclinic $Na_2Ti_3O_7$ crystals (JCPDS card No. 72-0148). The crystalline peaks at 24.2°, 28.4° and 48.1° are attributed to the (102), (111), and (020) crystallographic planes, respectively. In addition, no impurity peaks are observed in the NTO nanowires, indicating a pure monoclinic $Na_2Ti_3O_7$ phase. The diffraction peaks appearing at 37.8° and 44.3° are attributed to the (111) and (200) crystallographic planes of the Ag cubic phase (JCPDS card No. 04-0783), respectively. With increasing Ag content, the diffraction peaks at 40.0° and 63.0° of Ti crystals slowly disappear, and the diffraction peak at 37.8° is gradually enhanced. In addition, the positions of the peaks are almost identical, suggesting that the Ag NPs are deposited on the NTO surface instead of inside the lattice.

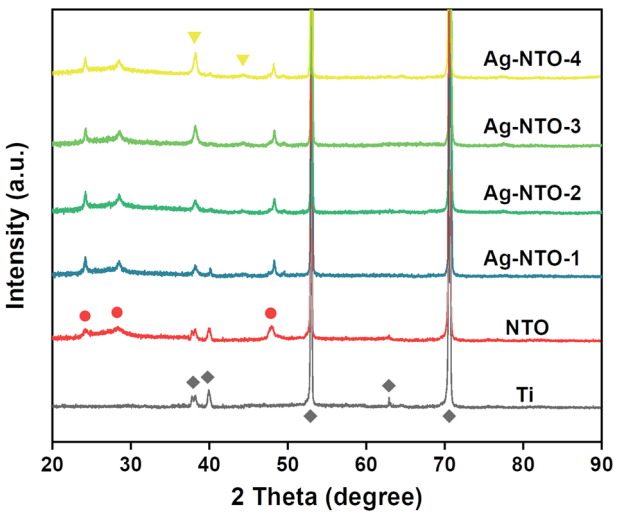

Fig. 1 XRD patterns of Ti sheet, NTO nanowires, and Ag-decorated NTO nanowires.

As shown in Fig. 2a, the scanning electron microscopy (SEM) image reveals that the surface of the original Ti substrate was clean and crack-free. After the hydrothermal reaction process with 1 M NaOH solution at 180 °C for 48 h, nanostructures consisting of $Na_2Ti_3O_7$ nanoflowers and nanowires (Fig. 2b) were obtained. The nanoflowers are almost perpendicular to the Ti substrate, indicating that they directly grew on the Ti sheet surface. The energy-dispersive X-ray spectroscopy (EDS) images in Fig. 2c show that the four elements Na, Ti, O, and Ag are uniformly distributed in the nanowires, which confirms the successful preparation of Ag-NTO composites. The TEM images in Fig. S1† show the lattice spacings and suggest that Ag NPs were deposited on the NTO surface rather than inside the lattice, as determined by XRD analysis.

The X-ray photoelectron spectroscopy (XPS) results further confirmed the surface elemental composition and chemical state of the Ag-NTO nanowires. As presented in Fig. 3a, C 1s (284.9 eV) was regarded as the internal marker for calibrating the binding energy. Fig. 3b shows the chemical states of O 1s, with the peaks at 530.6, 531.2, and 532.6 eV associated with O^{2-} species (O_L), oxygen vacancies (O_V) or defects in the lattice, and chemisorbed or dissociated oxygen species (O_C), respectively.[21,22] In Fig. 3c, the Ti 2p spin–orbit doublet peaks observed at 458.0 and 463.6 eV are related to the Ti^{4+} oxidation state.[23] As shown in Fig. 3d, the Ag peaks at 368.3 and 374.3 eV are attributed to Ag $3d_{5/2}$ and Ag $3d_{3/2}$, respectively. The spin energy is an eigenvalue of 6.0 eV, demonstrating the presence of Ag, not silver oxide, on the substrate surface.[24]

For the SERS performance evaluation, 4-MBA was used as a probe molecule. Fig. 4a shows the Raman spectra of MBA and NTO and the SERS spectra of MBA on NTO. The characteristic bands at 277, 444, and 700 cm^{-1} of NTO are attributed to $Na_2Ti_3O_7$.[25,26] The MBA molecule on NTO exhibits faint peaks at 613 and 1598 cm^{-1}, indicating the weak enhancement of NTO. Fig. 4b presents the SERS spectra of MBA adsorbed on the Ag-NTO substrates with different Ag sputtering powers obtained using 633 nm excitation light. The SERS activity gradually changes as the Ag sputtering power changes. The band assignments for the SERS spectra of the 4-MBA molecule are summarized in Table S1.† The slightly reduced Raman signal of Ag-NTO-4 is due to the excess Ag coverage, which leads to the disappearance of the hot spots.

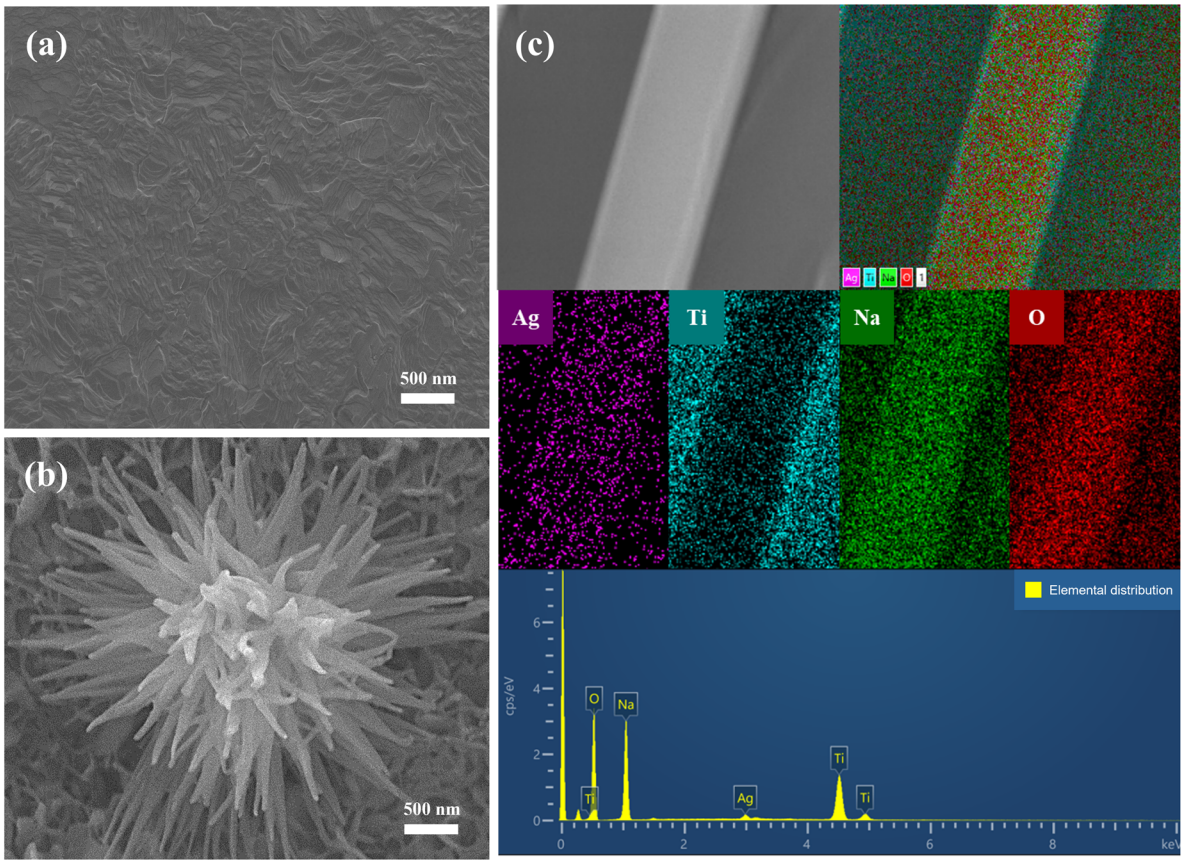

Fig. 2 SEM images of (a) an original Ti sheet and (b) grown NTO nanowires. (c) Elemental analysis of the Ag-NTO substrate.

The Ag-NTO-3 substrate was employed to further verify the SERS enhancement ability using MBA solutions with various concentrations ranging from 10^{-3} to 10^{-8} M. As shown in Fig. 4c, although the Raman intensity significantly decreases with decreasing probe concentration, the characteristic band is still observed at 10^{-8} M MBA, indicating the high SERS sensitivity of Ag-NTO-3. To investigate the changes in Raman spectra for various probe molecule concentrations, the relationship between the intensity of the Raman band at 1076 cm^{-1} and the MBA concentration was plotted. Fig. 4d presents a good linear relationship between the band intensity and probe molecule concentration, and the regression equation can be used for MBA concentration identification.

To quantify the Raman signal enhancement capability, the Raman band at 1076 cm^{-1} was selected, and the SERS enhancement factor (EF) was estimated according to the following equation:

$$EF = \frac{I_{SERS}}{I_{bulk}} \times \frac{N_{bulk}}{N_{SERS}} \quad (1)$$

where I_{SERS} and I_{bulk} are the SERS intensity of the band at 1076 cm^{-1} (MBA molecules adsorbed on the Ag-NTO-3 substrate) and Raman intensity of the band at 1098 cm^{-1} (solid MBA molecules), respectively. N_{SERS} and N_{bulk} are the corresponding numbers of probe molecules in the laser spot region. The number of probe molecules for the non-SERS substrates can be estimated by the following equation:

$$N_{bulk} = \left(\frac{N_A C V}{S_{sub}}\right) S_{laser} \quad (2)$$

where N_A is the Avogadro constant, C is the molar concentration of the solution (1.0×10^{-3} M), V is the volume of the droplet (100 μL), S_{sub} is the dispersion area of the solution on the substrate (spot diameter, 4 mm), and S_{laser} is the size of the laser spot (diameter, 1 μm). The number of probe molecules on the SERS substrate can be estimated by the following equation:

$$N_{SERS} = \frac{S_{laser}}{S_{MBA}}. \quad (3)$$

Here, S_{MBA} is the area occupied by a single MBA molecule, approximately 0.8 nm × 0.8 nm.[27] According to eqn (2) and (3), the values of N_{bulk} and N_{SERS} are 3.76×10^9 and 1.23×10^6, respectively. The calculated EF is approximately 6.9×10^7, suggesting excellent Raman enhancement of the Ag-NTO substrate.

Reproducibility is considered a critical parameter for the practical application of SERS sensing. For the NTO substrate, a uniform distribution of Ag NPs is very important for reproducibility because Ag decoration causes SPR and, as a result, SERS

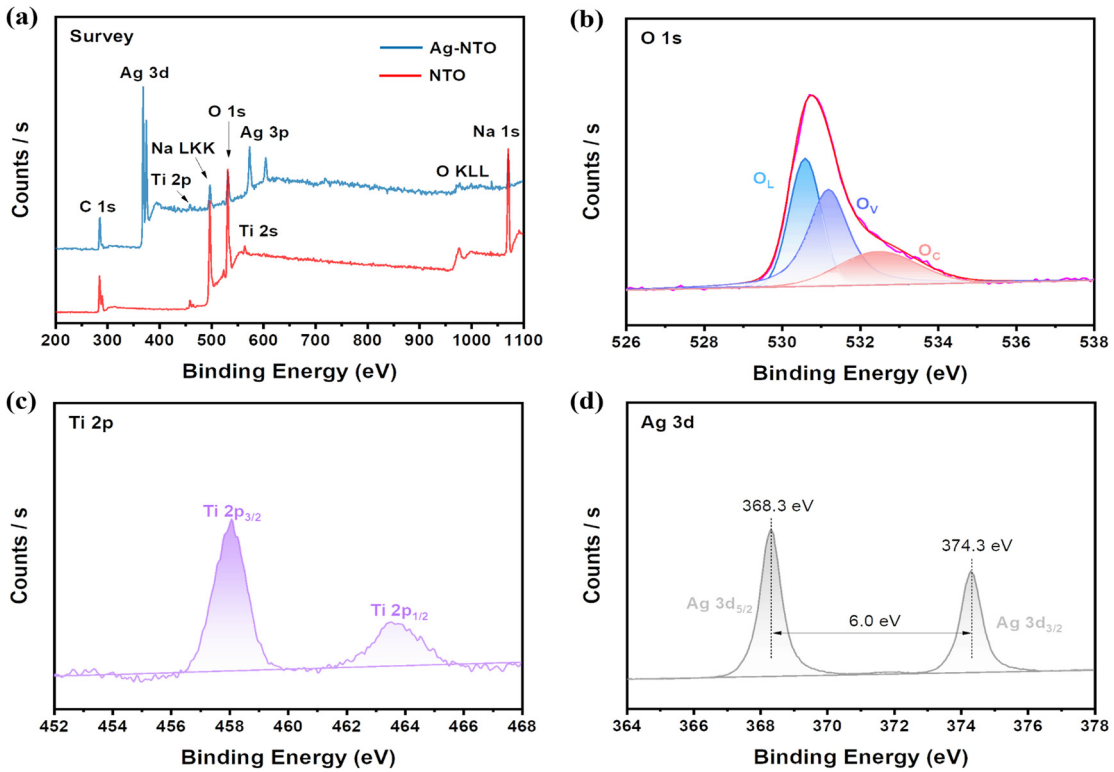

Fig. 3 XPS (a) survey, (b) O 1s, (c) Ti 2p, and (d) Ag 3d spectra for the Ag-NTO substrate.

"hot spots". Raman spectra collected from different points under the same experimental conditions were used to confirm the uniformity of the SERS substrate. Fig. 5a shows the SERS spectra of 10^{-3} M MBA adsorbed on the Ag-NTO-3 substrate obtained with 633 nm excitation light. Fig. 5b illustrates the calculated relative standard deviation (RSD) determined from the band intensity at 1076 cm^{-1}. The related SERS spectra under 514 nm excitation light is shown in Fig. S2.† The low RSD value indicates the excellent reproducibility of the SERS substrate.

The electromagnetic enhancement induced by LSPR on the noble metal surface plays a dominant role in the SERS sensitivity. NTO nanowires have a unique 3D dendritic structure that forms nanogaps ("hot spots") between the densely packed Ag NPs on their surface, resulting in a strong SPR that enhances the Raman signal. Fig. 6 shows SEM images of Ag-NTO substrates with different sputtering powers. The high-energy Ar atoms bombard the metal target to produce Ag NPs. The density of Ag NPs in the sputtering chamber is relatively small at an initial sputtering power of 10 W, so Ag NPs can be slowly and uniformly attached to the nanowire surface. As the sputtering power gradually increases, the concentration of Ag NPs increases, causing the scaled-up Ag particles to accumulate on the surface of the nanowire in the form of clusters. When the Ag sputtering power is further increased, the oversized aggregates of Ag NPs completely cover the surface of the nanowire and form a thicker Ag layer on its surface. The electromagnetic field enhancement on the NTO nanowires was confirmed using finite-difference time-domain (FDTD) simulations. The electromagnetic field intensity of the Ag-NTO structure increases with increasing sputtering power, and the highest intensity occurs at a sputtering power of 30 W. The Ag NPs are closely aligned on the NTO nanowires, forming many nanogaps, and the hot spots increase with the sputtering power. When the Ag sputtering power is further increasing, the oversized aggregates of Ag NPs completely cover the surface of the nanowire and form an Ag layer on its surface. The electromagnetic field intensity slightly decreases at a sputtering power of 40 W, which is due to the fact that the NPs accumulate so thickly that the nanogaps are filled when forming a Ag layer, weakening the "hot spot" effect. The FDTD analysis is in good agreement with the SERS results.

We further investigated the catalytic hydrogen production process similarly induced by photogenerated CT. FDTD analysis and SERS results demonstrated that a suitable Ag modification can maximize the LSPR enhancement. The enhanced localized electric field generated by LSPR boosts the electron–hole pair separation in the photocatalyst and increases the interband transition rate, making the energy higher than the bandgap of a semiconductor. The electrons are directed to the noble metal, while holes accumulate at the other edge of the semiconductor. The noble metal acts as an electron trap and reduces the recombination rate of electron–hole pairs. This process enhances the photoactivity of the photocatalyst. In contrast, too much noble metal reduces the active site in the reaction and becomes a recombination centre. High concen-

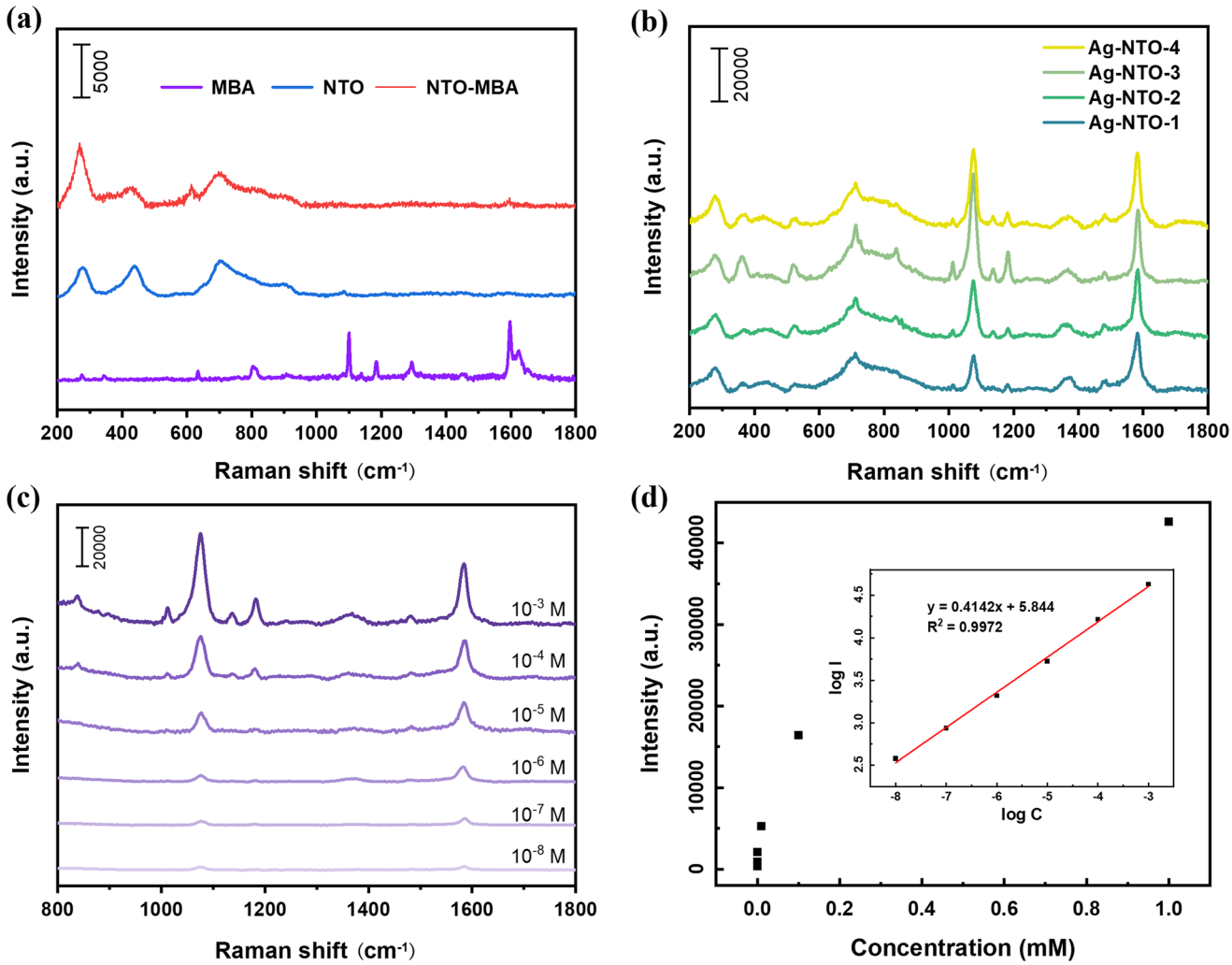

Fig. 4 (a) Raman spectra of MBA and NTO as well as SERS spectra of MBA on NTO. (b) SERS spectra of MBA adsorbed on Ag-NTO substrates with different Ag sputtering powers obtained using 633 nm excitation light. (c) SERS spectra of MBA solutions with various concentrations ranging from 10^{-3} to 10^{-8} M adsorbed on the Ag-NTO-3 substrate. (d) Linear relationship between the band intensity and probe molecule concentration.

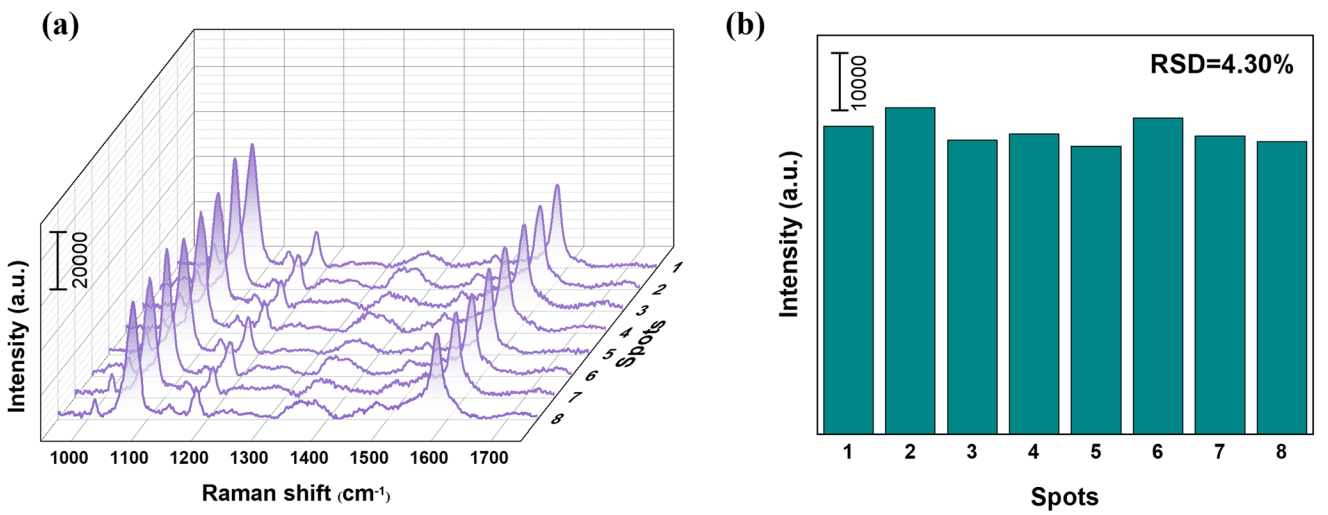

Fig. 5 (a) SERS spectra of 10^{-3} M MBA adsorbed on Ag-NTO-3 obtained with 633 nm excitation light. (b) RSD of the band intensity at 1076 cm^{-1}.

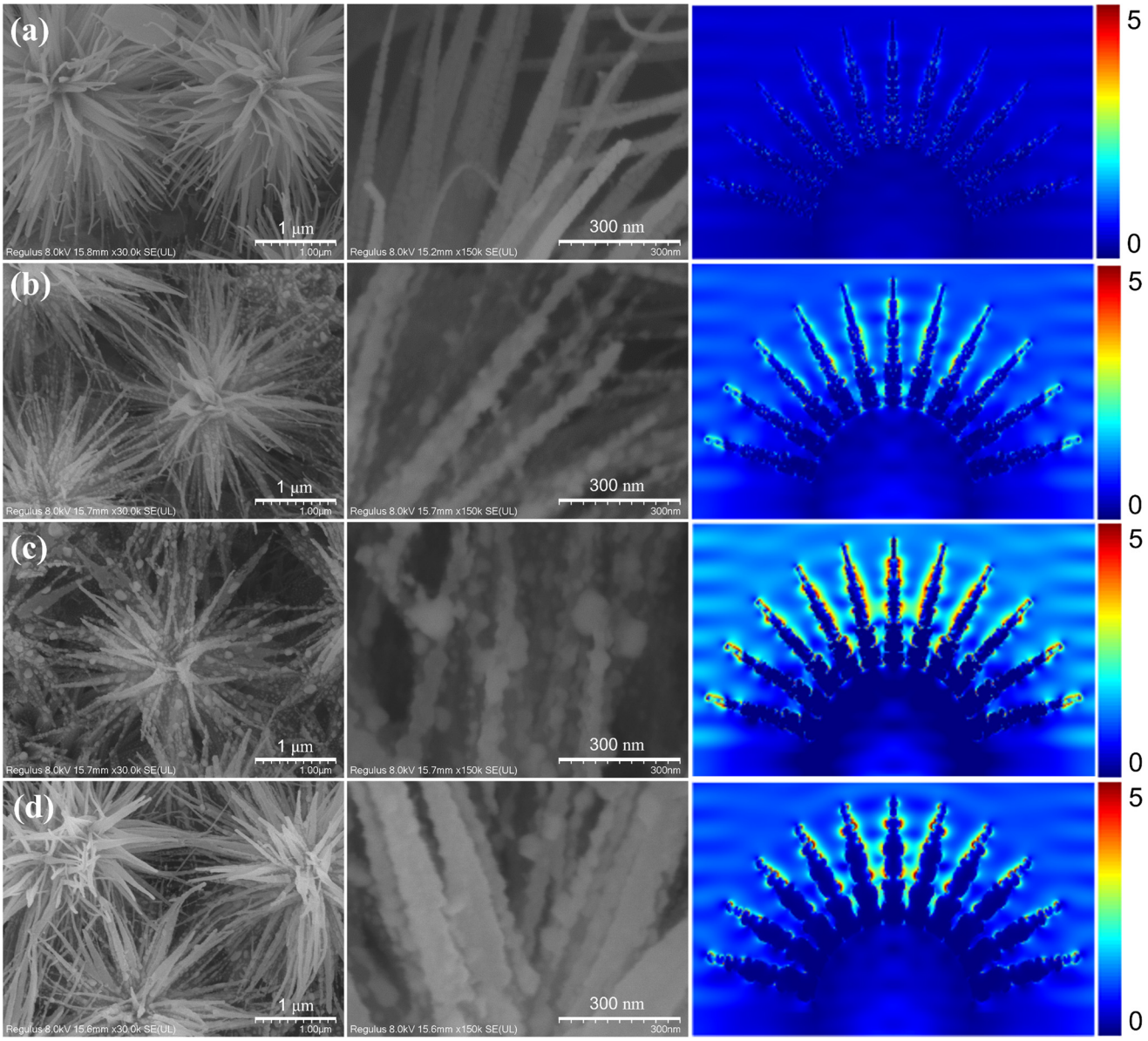

Fig. 6 High-magnification SEM images and electromagnetic field from FDTD simulations for (a) Ag-NTO-1, (b) Ag-NTO-2, (c) Ag-NTO-3, and (d) Ag-NTO-4 substrates.

tration of precious metals interferes with the active sites of the reaction. The enhanced PHE ability of the Ag-NTO-3 substrate was confirmed under visible-light irradiation ($\lambda > 420$ nm) and atmospheric pressure. As revealed in Fig. 7a, after Ag NPs are decorated on NTO nanowires, the PHE performance of Ag-NTO significantly increases. The H_2 production efficiency of the Ag-decorated substrate is 106.7 μmol h^{-1}, which is approximately 2 times than that of its counterpart (54.2 μmol h^{-1}) (Fig. 7b). The results demonstrate that sputtering Ag species can improve the photocatalytic hydrogen production performance of NTO nanowires.

Stability and reusability are also important parameters of the photocatalytic performance. Compared to powder photocatalysts, Ag-covered NTO nanowires grown on flake substrates present great advantages in terms of reusability. As shown in Fig. 7c, after four consecutive photocatalytic cycles, the hydrogen production rate of Ag-NTO nanowires decreases by 14%. As shown in Fig. S3,† there are no significant changes observed in the sea urchin-shaped nanostructure even after four PHE cycles. In addition, the XRD patterns and SERS spectra shown in Fig. 7d are basically consistent after four cycles, indicating the high reusability and stability of the photocatalysts.

As depicted in Fig. 8a, the PCR measurement results demonstrate the ability of Ag-NTO to rapidly separate charges at the interface and transfer photogenerated electrons. The Ag-covered nanowires present a much higher photocurrent density than NTO, which suggests a better efficiency of elec-

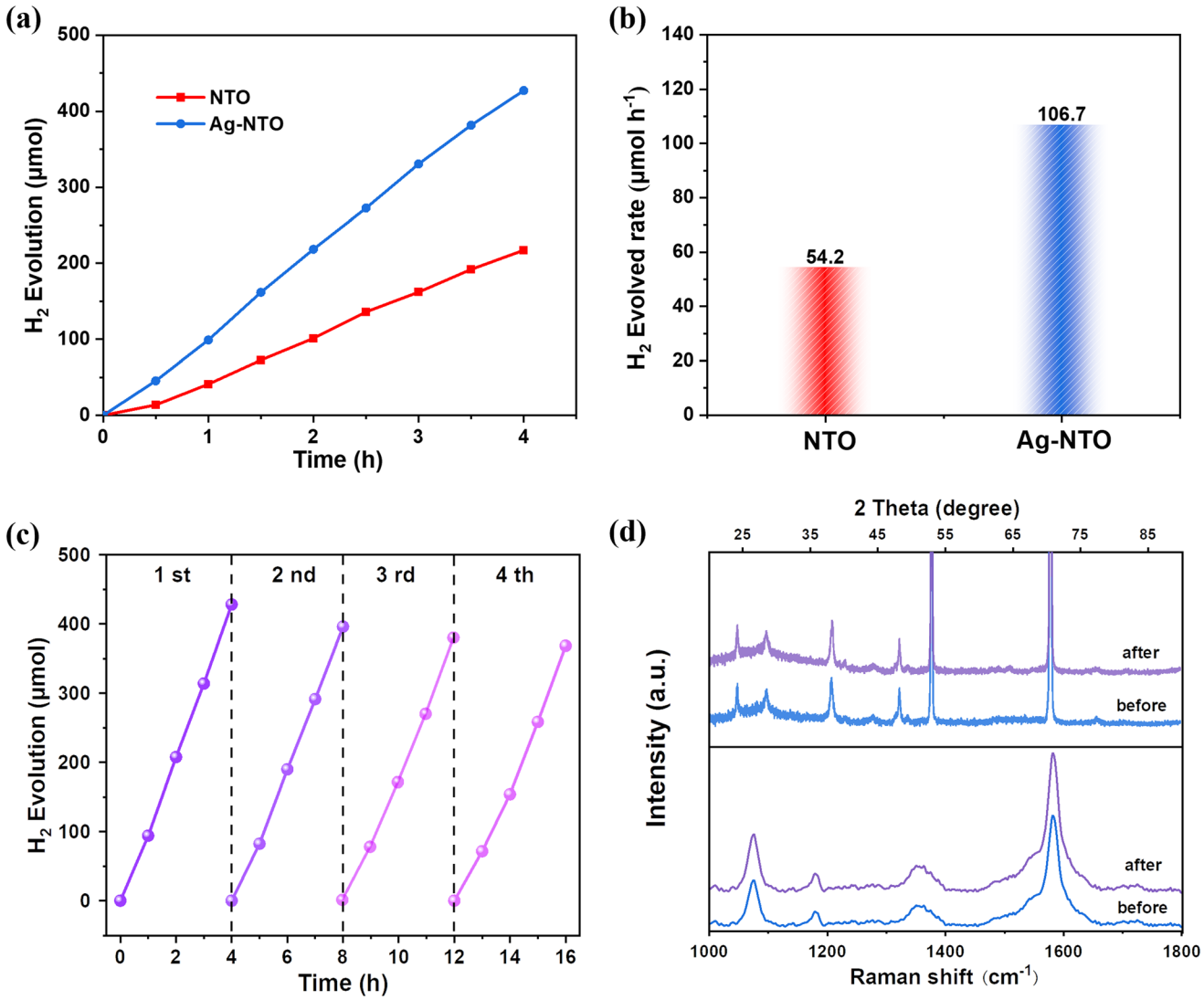

Fig. 7 (a) Photocatalytic hydrogen evolution and (b) evolution rate of NTO substrates. (c) Cycling experiment of PHE by Ag-NTO. (d) XRD patterns and SERS spectra of Ag-NTO before and after four cycles.

tron–hole pair transfer and separation. In addition, the corresponding EIS Nyquist plots in Fig. 8b illustrate the smaller electrochemical impedance radius of Ag-NTO. These results clearly indicate that Ag decoration directly affects the photocatalytic performance by weakening the interfacial CT resistance and promoting the efficiency of photogenerated carrier separation.[28]

Mott–Schottky (MS) measurements were used to estimate the band positions of the photocatalysts. As shown in Fig. 8c, the positive slopes of NTO and Ag-NTO indicate that both semiconductors are typical n-type semiconductors. Furthermore, the flat band potentials (E_f) of NTO and Ag-NTO are −0.30 and −0.52 V (*vs.* Ag/AgCl), respectively, which can be converted to −0.10 and −0.32 V (*vs.* NHE) ($E_{NHE} = E_{Ag/AgCl} + 0.197$).[29] As reported, the conduction band (CB) bottom potential of most n-type semiconductors is approximately 0.2 V lower than E_f, resulting in CB potentials (E_{CB}) of −0.30 and −0.52 V for NTO and Ag-NTO, respectively.[30] According to the empirical equation $E_{VB} = E_{CB} + E_g$ and the E_{VB} obtained from ultraviolet photoelectron spectroscopy (UPS) spectra (Fig. S4†), the band gaps of NTO and Ag-NTO can be calculated to be 3.22 and 3.04 eV, respectively. Based on the above discussion, we schematically present the band structure alignments of NTO and Ag-NTO. As shown in Fig. 8d, for the Ag-decorated substrate, the CB shifts upward, and the band gap narrows. The change trend favors the reduction of protons and the absorption of visible light, which improves the driving force for photocatalytic hydrogen production.[31]

Photoluminescence (PL) spectroscopy was performed to investigate the push–pull interaction and recombination of carriers or the energy band and electronic structures. The PHE reaction and PEC measurement confirm that NTO substrates can be excited to generate electron–hole pairs by illumination with a Xe lamp (λ > 420 nm). This is because O_V form a lower

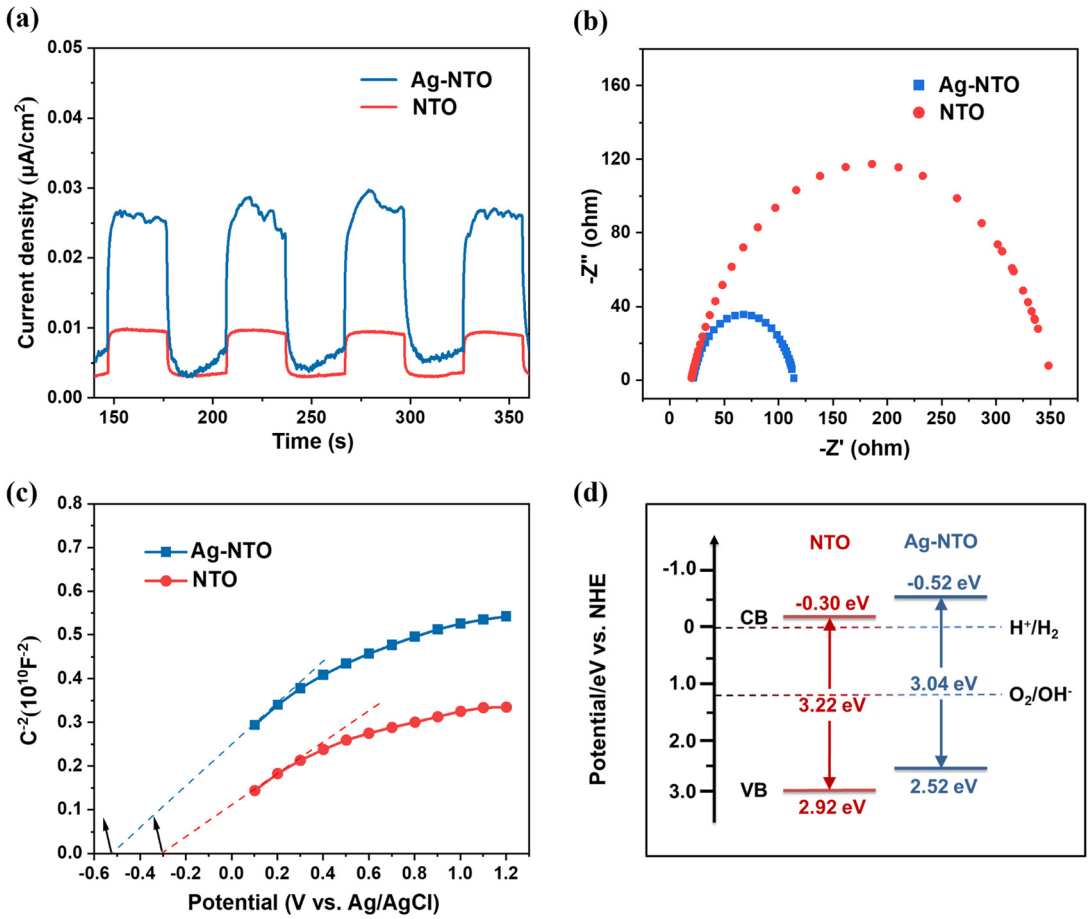

Fig. 8 (a) PCR, (b) EIS spectra, (c) M–S diagram, and (d) band alignment of substrates.

surface state level than the CB and improve visible light absorption in combination with the narrowed band gap, which explains the obtained results even though the maximum energy of the Xe lamp (2.96 eV) is insufficient for the band gap of the semiconductor.[32] Moreover, Ag was recognized to act as a bridge that leads to faster electron–hole transfer and separation rates and a lower recombination rate, which is attributed to the Schottky barrier formed at the junction due to the different work functions.[33] Fig. 9a shows the PL spectra of NTO substrates obtained with an ultraviolet (UV) laser of 220 nm. The wide emission peak of NTO at 490 nm suggests the existence of surface defects or oxygen vacancies.[34] The significant PL quenching phenomenon of Ag-NTO demonstrates that the recombination of electrons-holes in NTO can be significantly suppressed by Ag decoration.[20]

Fig. 9b shows the CT mechanism between MBA and Ag-NTO. In our previous works, we reported that the "hot electrons" of Ag NPs can be injected into the NTO valence band

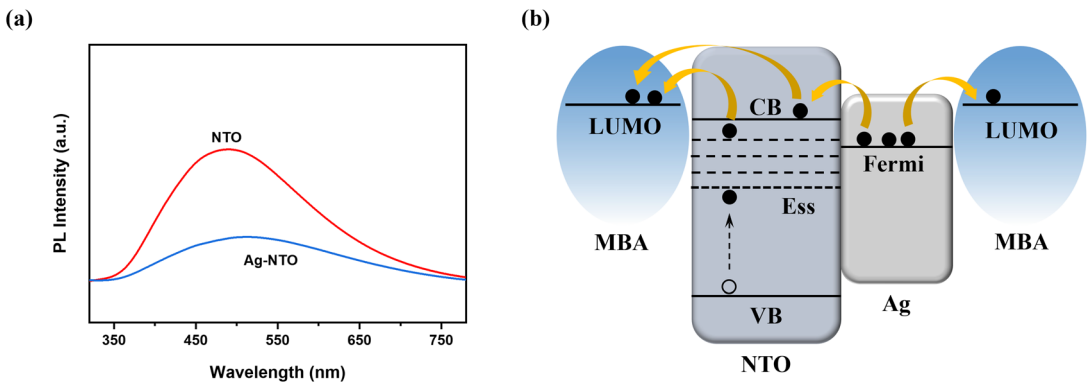

Fig. 9 (a) PL spectra of substrates. (b) Schematic of the CT mechanism between MBA and Ag-NTO.

(VB) and then transferred to the lowest unoccupied molecular orbital (LUMO) energy level of the adsorbed molecule or directly excited to the LUMO energy level of the MBA molecule to enhance the SERS signal.[35,36] In the system of MBA adsorbed on the Ag-NTO substrate, the Fermi level of Ag NPs is −4.84 eV, and the LUMO energy level of MBA is −3.21 eV.[37] The positions of the CB and VB energy levels according to E_{CB} and E_{VB} are −4.2 and −7.42 eV (*vs.* vacuum), respectively. The 633 (1.96 eV) and 514 nm (2.41 eV) excitation lasers can induce CT by overcoming the energy gap (1.63 eV) between the Fermi and LUMO levels. In addition, the photogenerated charge from the VB has been proven to be easily trapped by the surface state, and one of the releasing pathways is to transfer to the LUMO level of adsorbed molecules.[38–40] Several CT processes simultaneously affect the chemical enhancement mechanism and enhance the SERS sensitivity in combination with the electromagnetic contribution. The existence of O_V corresponds to narrow the band gap and less energy to the electron–hole pair separation, which improves the visible light absorption. As a result, higher interband transition rate and CT efficiency have enhanced the SERS and PHE performance.

4 Conclusions

In summary, we successfully prepared urchin-shaped Ag-NTO nanowires on a Ti sheet *via* the combination of hydrothermal reaction and magnetron sputtering. The proper Ag cover resulted in a tremendous SERS enhancement (EF = 6.9×10^7) owing to the cooperative contributions of SPR and CT. Further FDTD simulations suggested that Ag-NTO-3 had the highest electromagnetic field contribution, and the CT mechanism revealed a photoinduced CT process. The presence of O_V, confirmed by XPS and PL analysis, could form a deep energy level below the CB and improve visible light absorption in combination with the narrowed band gap. The better PHE performance of Ag-NTO was attributed to the fact that Ag decoration reduced the interfacial CT resistance and promoted the efficiency of photogenerated carrier separation. The repeated experiments validated the excellent stability and reusability of Ag-NTO as a photocatalyst and a SERS substrate. This work provides a novel approach for combining SERS and photocatalysis.

Author contributions

Lei Chen: methodology, formal analysis, writing – original draft; Yang Jin: formal analysis, writing – original draft; Shuang Guo: data curation; Eungyeong Park: data curation; Yunfei Xie: validation, funding acquisition; Young Mee Jung: funding acquisition, writing – review & editing.

Conflicts of interest

The authors declare no competing financial interest.

Acknowledgements

This work was supported by the Scientific Research Project of the Department of Education of Jilin Province (No. JJKH20220432KJ). This work was also supported by the National Research Foundation of Korea (NRF) grants funded by the Korea government (NRF-RS-2023-00271205, NRF-2020K2A9A2A06036299, and NRF-2021R1A2C2004550) and by Korea Basic Science Institute (National Research Facilities and Equipment Center) grant funded by the Ministry of Education (2020R1A6C101A195).

References

1 B. Han, N. Ma, S. Guo, J. Yu, L. Xiao, Y. Park, E. Park, S. Jin, L. Chen and Y. M. Jung, Size-dependent surface-enhanced Raman scattering activity of Ag@Cu_xOS yolk-shell nanostructures: surface plasmon resonance induced charge transfer, *J. Phys. Chem. C*, 2020, **124**, 16616–16623.
2 X. Wu, L. Luo, S. Yang, X. Ma, Y. Li, C. Dong, Y. Tian, L. Zhang, Z. Shen and A. Wu, Improved SERS nanoparticles for direct detection of circulating tumor cells in the blood, *ACS Appl. Mater. Interfaces*, 2015, **7**, 9965–9971.
3 Y. Liu, H. Ma, X. X. Han and B. Zhao, Metal-semiconductor heterostructures for surface-enhanced Raman scattering: synergistic contribution of plasmons and charge transfer, *Mater. Horiz.*, 2021, **8**, 370–382.
4 J. Wang, R. A. Ando and P. H. C. Camargo, Controlling the selectivity of the surface plasmon resonance mediated oxidation of p-aminothiophenol on Au nanoparticles by charge transfer from UV-excited TiO_2, *Angew. Chem., Int. Ed.*, 2015, **54**, 6909–6912.
5 Q. Ding, R. Li, M. Chen and M. Sun, Ag nanoparticles-TiO_2 film hybrid for plasmon-exciton co-driven surface catalytic reactions, *Appl. Mater. Today*, 2017, **9**, 251–258.
6 A. Rudola, K. Saravanan, C. W. Mason and P. Balaya, $Na_2Ti_3O_7$: an intercalation-based anode for sodium-ion battery applications, *J. Mater. Chem. A*, 2013, **1**, 2653.
7 K. Teshima, S. Lee, S. Murakoshi, S. Suzuki, M. Kiyohara, K. Yubuta, T. Shishido, M. Endo and S. Oishi, A Unique Three-Dimensional Photocatalytic Structure Consisting of Highly Crystalline $Na_2Ti_3O_7$ Whiskers Grown from a NaCl Flux, *Cryst. Growth Des.*, 2010, **10**, 2533–2540.
8 A. Musumeci, D. Gosztola, T. Schiller, N. M. Dimitrijevic, V. Mujica, D. Martin and T. Rajh, SERS of Semiconducting Nanoparticles (TiO_2 Hybrid Composites), *J. Am. Chem. Soc.*, 2009, **131**, 6040–6041.
9 S. Linic, P. Christopher and D. B. Ingram, Plasmonic-metal nanostructures for efficient conversion of solar to chemical energy, *Nat. Mater.*, 2011, **10**, 911–921.
10 N. Keller, J. Ivanez, J. Highfield and A. M. Ruppert, Photo-/thermal synergies in heterogeneous catalysis: Towards low-temperature (solar-driven) processing for sustainable energy and chemicals, *Appl. Catal. B-Environ.*, 2021, **296**, 120320.

11 Z. Mao, H. Vang, A. Garcia, A. Tohti, B. J. Stokes and S. C. Nguyen, Carrier diffusion-the main contribution to size-dependent photocatalytic activity of colloidal gold nanoparticles, *ACS Catal.*, 2019, **9**, 4211–4217.
12 A. Sclafani, M.-N. Mozzanega and P. Pichat, Effect of silver deposits on the photocatalytic activity of titanium dioxide samples for the dehydrogenation or oxidation of 2-propanol, *J. Photoch. Photobio. A*, 1991, **59**, 181–189.
13 B. Neppolian, A. Bruno, C. L. Bianchi and M. Ashokkumar, Graphene oxide-based Pt-TiO_2 photocatalyst: ultrasound assisted synthesis, characterization and catalytic efficiency, *Ultrason. Sonochem.*, 2012, **19**, 9–15.
14 J. Prakash, P. Kumar, R. A. Harris, C. Swart, J. H. Neethling, A. J. Van Vuuren and H. C. Swart, Synthesis, characterization and multifunctional properties of plasmonic Ag-TiO_2 nanocomposites, *Nanotechnology*, 2016, **27**, 355707.
15 M. Es-Souni, M. Es-Souni, S. Habouti, N. Pfeiffer, A. Lahmar, M. Dietze and C.-H. Solterbeck, Brookite formation in TiO_2 Ag nanocomposites and visible-light-induced templated growth of Ag nanostructures in TiO_2, *Adv. Funct. Mater.*, 2010, **20**, 377–385.
16 S. Khanam and S. K. Rout, Plasmonic Metal/Semiconductor Heterostructure for Visible Light Enhanced H_2 Production, *ACS Omega*, 2022, **7**, 25466–25475.
17 J. Yang, G. Song, L. Zhou, X. Wang, L. You and J. Li, Highly sensitively detecting tetramethylthiuram disulfide based on synergistic contribution of metal and semiconductor in stable Ag/TiO_2 core-shell SERS substrates, *Appl. Surf. Sci.*, 2021, **539**, 147744.
18 A. A. Yadav, Y. M. Hunge, A. G. Dhodamani and S.-W. Kang, Hydrothermally Synthesized Ag@MoS_2 Composite for Enhanced Photocatalytic Hydrogen Production, *Catalysts*, 2023, **13**, 716.
19 T. Cong, Y. Huang, Y. Zhao, H. Huang, D. Zhang, C. Li, Z. Fan and L. Pan, Extremely sensitive and reusable surface-enhanced Raman scattering substrate based on 3D Ag-titanium dioxide nanowires, *J. Alloys Compd.*, 2021, **859**, 158389.
20 C.-Y. Xu, J. Wu, P. Zhang, S.-P. Hu, J.-X. Cui, Z.-Q. Wang, Y.-D. Huang and L. Zhen, Molten salt synthesis of $Na_2Ti_3O_7$ and $Na_2Ti_6O_{13}$ one-dimensional nanostructures and their photocatalytic and humidity sensing properties, *CrystEngComm*, 2013, **15**, 3448.
21 X.-G. Han, H.-Z. He, Q. Kuang, X. Zhou, X.-H. Zhang, T. Xu, Z.-X. Xie and L.-S. Zheng, Controlling Morphologies and Tuning the Related Properties of Nano/Microstructured ZnO Crystallites, *J. Phys. Chem. C*, 2009, **113**, 584–589.
22 J. Wang, Z. Wang, B. Huang, Y. Ma, Y. Liu, X. Qin, X. Zhang and Y. Dai, Oxygen Vacancy Induced Band-Gap Narrowing and Enhanced Visible Light Photocatalytic Activity of ZnO, *ACS Appl. Mater. Interfaces*, 2012, **4**, 4024–4030.
23 J. Du, J. Zhang, Z. Liu, B. Han, T. Jiang and Y. Huang, Controlled synthesis of Ag/TiO_2 core shell nanowires with smooth and bristled surfaces via a one-step solution route, *Langmuir*, 2006, **22**, 1307–1312.
24 G. B. Hoflund, Z. F. Hazos and G. N. Salaita, Surface characterization study of Ag, AgO, and Ag_2O using X-ray photoelectron spectroscopy and electron energy-loss spectroscopy, *Phys. Rev. B*, 2000, **62**, 11126–11133.
25 Y. Cao, Q. Ye, F. Wang, X. Fan, L. Hu, F. Wang, T. Zhai and H. Li, A new triclinic phase $Na_2Ti_3O_7$ anode for sodium-ion battery, *Adv. Funct. Mater.*, 2020, **30**, 2003733.
26 A. Turki, H. Kochkar, C. Guillard, G. Berhault and A. Ghorbel, Effect of Na content and thermal treatment of titanate nanotubes on the photocatalytic degradation of formic acid, *Appl. Catal. B-Environ.*, 2013, **138–139**, 401–415.
27 T. A. Laurence, G. B. Braun, N. O. Reich and M. Moskovits, Robust SERS Enhancement Factor Statistics Using Rotational Correlation Spectroscopy, *Nano Lett.*, 2012, **12**, 2912–2917.
28 S. V. P. Vattikuti, P. A. K. Reddy, P. C. NagaJyothi, J. Shim and C. Byon, Hydrothermally synthesized $Na_2Ti_3O_7$ nanotube-V_2O_5 heterostructures with improved visible photocatalytic degradation and hydrogen evolution-Its photocorrosion suppression, *J. Alloys Compd.*, 2018, **740**, 574–586.
29 X. Song, X. Zhang, X. Li, H. Che, P. Huo, C. Ma, Y. Yan and G. Yang, Enhanced light utilization efficiency and fast charge transfer for excellent CO_2 photoreduction activity by constructing defect structures in carbon nitride, *J. Colloid Interf. Sci.*, 2020, **578**, 574–583.
30 J. Xu, X. Yan, Y. Qi, Y. Fu, C. Wang and L. Wang, Novel phosphidated MoS_2 nanosheets modified CdS semiconductor for an efficient photocatalytic H_2 evolution, *Chem. Eng. J.*, 2019, **375**, 122053.
31 X. Zhao, Y. Zhang, X. Zhao, X. Wang, Y. Zhao, H. Tan, H. Zhu, W. Ho, H. Sun and Y. Li, Urea and melamine formaldehyde resin-derived tubular g-C_3N_4 with highly efficient photocatalytic performance, *ACS Appl. Mater. Interfaces*, 2019, **11**, 27934–27943.
32 M. Kolaei, M. Tayebi, Z. Masoumi, A. Tayyebi and B.-K. Lee, Optimal growth of sodium titanate nanoflower on TiO_2 thin film for the fabrication of a novel Ti/TiO_2/$Na_2Ti_3O_7$ photoanode with excellent stability, *J. Alloys Compd.*, 2022, **913**, 165337.
33 G. Shan, S. Zheng, S. Chen, Y. Chen and Y. Liu, Multifunctional ZnO/Ag nanorod array as highly sensitive substrate for surface enhanced Raman detection, *Colloids Surf., B*, 2012, **94**, 157–162.
34 Y.-C. Chang, J.-C. Lin and C.-M. Chou, $H_2Ti_3O_7$ nanowires as a high-performance photocatalytic and surface-enhanced Raman scattering substrate, *J. Photoch. Photobio. A*, 2020, **400**, 112666.
35 B. Han, L. Chen, S. Jin, S. Guo, J. Park, H. S. Yoo, J. H. Park, B. Zhao and Y. M. Jung, Modulating Mechanism of the LSPR and SERS in Ag/ITO Film: Carrier Density Effect, *J. Phys. Chem. Lett.*, 2021, **12**, 7612–7618.
36 X.-Y. Zhang, L. Chen, Y. Wang, Y. Zhang, J. Yang, H. C. Choi and Y. M. Jung, Design of tunable ultraviolet (UV) absorbance by controlling the Ag-Al co-sputtering deposition, *Spectrochim. Acta A*, 2018, **197**, 37–42.

37 X. Zhang, Z. Yu, W. Ji, H. Sui, Q. Cong, X. Wang and B. Zhao, Charge-transfer effect on surface-enhanced Raman scattering (SERS) in an ordered Ag NPs/4-Mercaptobenzoic Acid/TiO_2 system, *J. Phys. Chem. C*, 2015, **119**, 22439–22444.
38 X. Zhao, W. Zhang, C. Peng, Y. Liang and W. Wang, Sensitive surface-enhanced Raman scattering of TiO_2/Ag nanowires induced by photogenerated charge transfer, *J. Colloid Interf. Sci.*, 2017, **507**, 370–377.
39 X. Fan, M. Li, Q. Hao, M. Zhu, X. Hou, H. Huang, L. Ma, O. G. Schmidt and T. Qiu, High SERS sensitivity enabled by synergistically enhanced photoinduced charge transfer in amorphous nonstoichiometric semiconducting films, *Adv. Mater. Interfaces*, 2019, **6**, 1901133.
40 L. Yang, X. Jiang, W. Ruan, J. Yang, B. Zhao, W. Xu and J. R. Lombardi, Charge-transfer-induced surface-enhanced Raman scattering on Ag-TiO_2 Nanocomposites, *J. Phys. Chem. C*, 2009, **113**, 16226–16231.